High-range-resolution imaging using frequency domain interferometry with stabilization techniques for real-time vascular ultrasound

Hirofumi Taki[1*], Kousuke Taki[2], Makoto Yamakawa[3], Tsuyoshi Shiina[4], Motoi Kudo[2], and Toru Sato[5]

[1]Graduate School of Engineering, Tohoku University, Sendai 980-8579, Japan
[2]Department of Anatomy, Shiga University of Medical Science, Otsu 520-2192, Japan
[3]Advanced Biomedical Engineering Research Unit, Kyoto University, Kyoto 606-8501, Japan
[4]Graduate School of Medicine, Kyoto University, Kyoto 606-8501, Japan
[5]Graduate School of Informatics, Kyoto University, Kyoto 606-8501, Japan
E-mail: taki@ecei.tohoku.ac.jp

In the present study, we employed two techniques to acquire high-range-resolution images of human carotid arteries in vivo using frequency domain interferometry and the Capon method. One technique ensures the robust depiction of artery interfaces; the other suppresses the deterioration of the imaging performance due to variation of the echo waveform. We applied the proposed method to raw data obtained using a commercial ultrasonographic device with a 7.5 MHz linear array probe. Our method succeeded to depict a horizontal 0.15-mm-thick agar membrane stably, and the standard deviation of the estimated depth was suppressed to 26.7% of that obtained using the conventional method. Our method also succeeded in acquiring high-range-resolution images of six human carotid arteries in vivo. Requiring 0.06 s on a desktop PC with a single CPU for a 1 × 2 cm region of interest, our method is suitable for real-time imaging. © 2015 The Japan Society of Applied Physics

1. Introduction

Cardiovascular disease remains a substantial cause of mortality.[1] The assessment of cardiac function is one of the main clinical issues.[2–5] Another clinical issue is arterial plaques whose rupture or erosion leads to abrupt thrombosis, and the urgent demand is how to establish a marker of vulnerable plaques.[6] Transcutaneous ultrasound B-mode imaging is widely used to detect plaques in carotid arteries.[7] Thus, improving the spatial resolution of imaging would bring a major advancement in identification of high-risk plaques.[8] Other trials focus on the measurement of carotid arterial stiffness.[9–11] Carotid artery wall thickness, known as the carotid intima-media thickness (CIMT), determined by ultrasonography (US), is also a measure of early atherosclerosis.[9,12,13] Because these measures of arterial stiffness lack sufficient reliability for clinical routine applications,[14] improvement in the range resolution of US is needed to establish more reliable markers of cardiovascular risk.

Using a higher transmit frequency improves the spatial and contrast resolutions because narrower beam and pulse widths can be used; however, a high-frequency pulse is rapidly attenuated, limiting its practicality.[15] Alternatively, tissue harmonic imaging and spatial compound imaging suppress speckle noise and consequently improve the contrast and spatial resolution. However, it is difficult to acquire a range resolution higher than one-half the pulse length because each of these modes generally uses a data-independent delay-and-sum beamformer with a set of predetermined weights.[15]

In the field of radio imaging, since the 1960s, adaptive beamforming algorithms have been proposed to improve spatial resolution without using high transmit frequencies. One common technique is the use of a Capon beamformer, which uses a set of weights calculated by minimizing the output power, subject to the constraint that a desired signal gives a constant response.[16] In US, signals from different targets strongly correlate. Therefore, strategies involving output-power minimization do not work because the interference signals cancel the desired signal.[17,18] Spatial-averaging techniques suppress the cross-correlation between the signals from different targets.[19,20] Thus, several groups have used the Capon method with spatial averaging to improve the lateral resolution in US.[21–23] Another approach is the use of eigenvalue adaptive beamforming algorithms.[24,25] Because these methods introduced the assumption that the targets are modeled as points, the grid size should be small enough to achieve sufficient spatial resolution and robustness. However, this incurs high computational cost, indicating the difficulty of using these methods with real-time signal processing. They also require high signal-to-noise ratio (SNR) conditions.

Frequency domain interferometry (FDI) imaging has been proposed to improve the range resolution in atmospheric radar[26] and optical coherence tomography;[27] however, these methods involve the use of narrow-band signals, and thus blind application of these methods to US is unlikely to succeed. In a previous study, we proposed a high range resolution method based on FDI with an adaptive beamforming algorithm.[28,29] This method employed several techniques to deal with the broadband signals and succeeded in acquiring an image of a swine femoral artery with high range resolution. However, optimization of the parameter settings received little attention.

Our goal is to realize the practical use of the high-range-resolution imaging for screening early signs of atherosclerosis and for detecting the position and shape of a plaque correctly. The presence of coherent interference reduces the performance of conventional FDI imaging to a great extent in terms of estimating echo intensity than in terms of spatial resolution.[23] Conventional FDI imaging has insufficient accuracy in estimating echo intensity, resulting in a lower continuity for images in the lateral direction than in the case of conventional B-mode imaging. We previously found the necessity of employing frequency averaging to suppress coherent interference in a simple simulation study without noise.[29] However, FDI imaging employing the conventional frequency averaging technique requires two conditions; the first is a high SNR and the second is that the echo waveform returned from each target is almost the same as the waveform

of the reference signal.[30] We have investigated the effects of the bandwidths used for frequency averaging and for imaging on the performance of FDI imaging in terms of estimating echo intensity, and proposed the frequency averaging stabilization technique that ensure the robust depiction of artery interfaces when there is a thin layer close to the arterial wall.[31] We also proposed the reference compound technique that suppresses the deterioration of FDI imaging performance due to variation of the echo waveform.[32] In this study, we apply FDI imaging with the two proposed techniques to an agar membrane, a swine femoral artery in vitro, and six living human carotid arteries in vivo. We explain the methods, present experimental results obtained using a commercial US device, and form conclusions related to our findings.

2. Materials and methods

The method presented is based on FDI with the Capon method, which is an adaptive beamforming algorithm. To improve the range resolution in US, we apply this method to each individual scan line of the radio frequency (RF) data reconstructed from the in-phase and quadrature (IQ) data.[29] In this section, we briefly describe FDI and the Capon method, and subsequently propose a technique that suppresses the deterioration in FDI imaging performance due to the echo waveform variation. Finally, we explain a robust imaging technique that we call the reference compound technique.

2.1 FDI imaging with the Capon method

FDI imaging is used to estimate the intensity of an echo that returned from a desired depth. This method transforms the received signal that returned from a region of interest (ROI) to that in the frequency domain and sums the frequency components of the signal after phase compensation. The phase of each component of the echo that returned from a given depth depends on the product of the frequency of the component and the depth. Therefore, FDI imaging employs phase compensation to integrate the frequency components of the echo that returned from the desired depth coherently.[29]

The application of the Capon method requires that all the frequency components of the echo from a single target have the same intensity. To fulfill the requirements for ultrasound imaging, we apply the whitening technique, which assumes that the echo that returned from a single target resembles the reference signal in waveform, and normalizes the frequency components of the received signal with the reference signal:

$$X_{Hk} = X_{Pk} X_{Rk}^* / (|X_{Rk}|^2 + \eta), \quad (1)$$

where η is a term for stabilization, and X_{Hk}, X_{Pk}, and X_{Rk} are the k-th frequency components of the received RF data after whitening, the received RF data before whitening, and a reference signal of the RF data without whitening, respectively. In this study, we use the RF data of 1 cm width in each scan line after a common delay and sum process, where we employ a rectangular window function in the time domain, as we did in our previous work.[29]

The Capon method suppresses the contribution of the echoes that returned from targets at undesired depths, subject to a constant response at the desired depth. This problem is expressed as
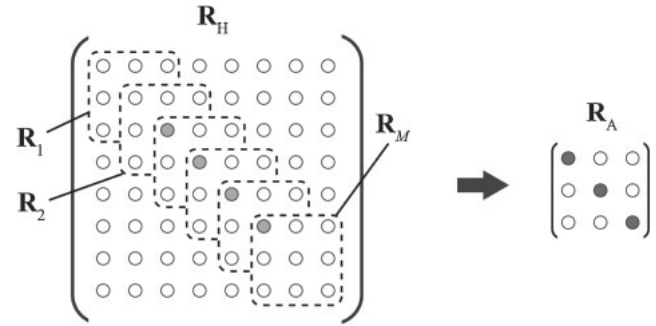

Fig. 1. Schema of the frequency averaging technique. Colored diagonal elements of the covariance matrix $\mathbf{R}_H$ are distributed among the diagonal elements of the covariance matrix after frequency averaging $\mathbf{R}_A$.

$$\text{minimize } P = \mathbf{W}^{T*} \mathbf{R}_H \mathbf{W} \text{ subject to } \mathbf{C}^{T*} \mathbf{W} = 1, \quad (2)$$

$$\mathbf{R}_H = \mathbf{X}_H \mathbf{X}_H^{T*}, \quad (3)$$

$$\mathbf{X}_H = \begin{bmatrix} X_{H1} & X_{H2} & \cdots & X_{HN} \end{bmatrix}^T, \quad (4)$$

$$\mathbf{C} = \begin{bmatrix} e^{jk_1 r} & e^{jk_2 r} & \cdots & e^{jk_N r} \end{bmatrix}^T, \quad (5)$$

where k_l is the l-th wavenumber of the frequency components used by FDI imaging, $r/2$ is the desired depth, and $[\cdot]^*$ and $[\cdot]^T$ denote the complex conjugate and the transpose, respectively. Because $P = \mathbf{W}^{T*} \mathbf{R}_H \mathbf{W} = |\mathbf{W}^{T*} \mathbf{X}_H|^2$, P is the echo intensity of the frequency components that are summed coherently using the weighting vector $\mathbf{W}$. The constraint in Eq. (2) guarantees a constant contribution from the echo that returned from a target located at the desired depth of $r/2$. The minimization problem of Eq. (2) can be solved by the application of Lagrange multiplier methods without the calculation of the optimum weighting vector. The solution of Eq. (2) is given by

$$P_{\text{Cap}}(r) = \frac{1}{\mathbf{C}^{T*} \mathbf{R}_H^{-1} \mathbf{C}}, \quad (6)$$

where $\mathbf{R}_H^{-1}$ denotes the inverse matrix of $\mathbf{R}_H$.[26]

2.2 Frequency averaging for a stabilized beam pattern

Frequency averaging has been used to suppress the correlation between the echoes that returned from different depths,[26,29] similar to the spatial averaging employed by spatial domain interferometry imaging.[20] We have theoretically investigated the effect of the bandwidths used for frequency averaging and for imaging on the performance of FDI imaging in estimating echo intensity, and propose a technique that ensure the robust depiction of artery interfaces when there is a thin layer close to the arterial wall.[31] When the bandwidth for frequency averaging is wider than that for imaging, the frequency components, which have frequencies close to the center frequency, are distributed among the covariance matrix uniformly, as shown in Fig. 1. This smoothes out the excessive suppression of the echo intensity estimated by the Capon method. We call this technique frequency averaging stabilization (FAS).[31] In this section, we first describe the process of frequency averaging, and subsequently explain the effect of FAS.

This technique averages the submatrices of the covariance matrix of the received signal along the diagonal direction. The covariance matrix after frequency averaging is given by

$$\mathbf{R}_\mathrm{A} = \frac{1}{M}\sum_{m=1}^{M}\mathbf{R}_m, \tag{7}$$

$$R_{mij} = X_{\mathrm{H}(i+m-1)}X^*_{\mathrm{H}(j+m-1)}, \tag{8}$$

where R_{mij} is the (i, j) element of the m-th submatrix $\mathbf{R}_m$, and M is the number of submatrices.

After applying whitening and frequency averaging to the received signal, the intensity estimated by FDI imaging with the Capon method expressed in Eq. (2) is modified as

$$\text{minimize } P'(r) = \mathbf{W}^{\mathrm{T}*}_\mathrm{A}\mathbf{R}_\mathrm{A}\mathbf{W}_\mathrm{A} \text{ subject to } \mathbf{C}^{\mathrm{T}*}_\mathrm{A}\mathbf{W}_\mathrm{A} = 1, \tag{9}$$

$$\mathbf{C}_\mathrm{A} = \begin{bmatrix} \exp(jk_1r) & \exp(jk_2r) & \cdots & \exp(jk_{N-M+1}r) \end{bmatrix}^{\mathrm{T}}, \tag{10}$$

where $\mathbf{W}_\mathrm{A}$ is a modified weighting vector of size $L = N - M + 1$. The intensity estimated by FDI imaging, using an appropriate weighting vector $\mathbf{W}_\mathrm{A}$ acquired by the Capon method, is

$$P'_\mathrm{Cap}(r) = \frac{1}{\mathbf{C}^{\mathrm{T}*}_\mathrm{A}(\mathbf{R}_\mathrm{A} + \eta'\mathbf{E})^{-1}\mathbf{C}_\mathrm{A}}, \tag{11}$$

where $\eta'\mathbf{E}$ is a diagonal loading matrix used to avoid instability in the calculation of the inverse matrix.[29]

In a previous study, frequency averaging is used to suppress the correlation between echoes from different targets.[29] Frequency averaging assumes that the frequency component of the received RF data after whitening is expressed by

$$X_{\mathrm{H}i} = \sum_o \alpha_o \exp(-jk_ir_o), \tag{12}$$

$$k_i = k_1 + (i-1)\Delta k, \tag{13}$$

where α_o is the amplitude of the echo that returned from the o-th target, $r_o/2$ is the target depth of the o-th target, and Δk is the wavenumber of the sampling frequency interval. In this case, an element of the covariance matrix after frequency averaging is given by

$$\begin{aligned}
R_{\mathrm{A}ij} &= \frac{1}{M}\sum_{m=1}^{M} X_{\mathrm{H}(i+m-1)}X^*_{\mathrm{H}(j+m-1)} \\
&= \sum_o |\alpha_o|^2 \exp\{-j(i-j)\Delta kr_o\} + g_{ij}, \tag{14}
\end{aligned}$$

$$\begin{aligned}
g_{ij} &= \sum_{o_1,o_2} \alpha_{o_1}\alpha_{o_2} \frac{1}{M}\sum_{m=1}^{M} \exp(-jk_{i+m-1}r_{o_1} + jk_{j+m-1}r_{o_2}) \\
&= \sum_{o_1,o_2} \alpha_{o_1}\alpha_{o_2} \exp\{-j(i-j)\Delta kr_{o_1}\} \\
&\quad \times \frac{1}{M}\sum_{m=1}^{M} \exp(jk_{j+m-1}\Delta r) \tag{15} \\
&\cong \sum_{o_1,o_2} \alpha_{o_1}\alpha_{o_2} \exp\{-j(i-j)\Delta kr_{o_1}\} \\
&\quad \times \exp\{j(k_j + M\Delta k/2)\Delta r\}\frac{\sin(M\Delta k\Delta r/2)}{M\Delta k\Delta r/2},
\end{aligned}$$

$$\Delta r = r_{o_2} - r_{o_1}, \tag{16}$$

where $R_{\mathrm{A}ij}$ is the (i, j) element of the covariance matrix after frequency averaging $\mathbf{R}_\mathrm{A}$, g_{ij} is the cross-correlation term, and $\Delta r/2$ is the target interval between o_1 and o_2. The proposed method assumes that multiple flat interfaces exist in a ROI, and in this case, the proposed method depicts sharp peaks at the target depths. Therefore, in arterial wall imaging the target interval denotes the interval between two interfaces.

Equation (15) shows that the cross-correlation term g_{ij} is suppressed in proportion to a sinc function:

$$g_{ij} \propto \frac{\sin(M\Delta k\Delta r/2)}{M\Delta k\Delta r/2} = \frac{\sin(\pi B_\mathrm{A}\Delta r/c)}{\pi B_\mathrm{A}\Delta r/c}, \tag{17}$$

where $B_\mathrm{A} = M\Delta k$ is the bandwidth for frequency averaging, and c is the speed of sound. The bandwidth for imaging B_I is given by $L\Delta k$. We use the whole bandwidth B for frequency averaging and imaging, i.e., $B = B_\mathrm{A} + B_\mathrm{I}$. The conventional FDI imaging allocates one-half of the whole bandwidth for frequency averaging.

FAS allocates a wide bandwidth for frequency averaging to improve the performance of FDI imaging in estimating echo intensity, and predicts the underestimation of echo intensity in FDI imaging at its worst. When the bandwidth for frequency averaging is wider than that for imaging, i.e., when the size of the submatrix L is smaller than the number of submatrices M, the diagonal elements of the covariance matrix $\mathbf{R}_\mathrm{H}$, which has frequencies close to the center frequency, are distributed along the diagonal elements of the covariance matrix after frequency averaging $\mathbf{R}_\mathrm{A}$, as shown in Fig. 1. The additive value to each diagonal element of the covariance matrix $\mathbf{R}_\mathrm{A}$ is expressed by

$$\begin{aligned}
\frac{1}{M}\sum_{l=L}^{M} X_{\mathrm{H}l}X^*_{\mathrm{H}i} &\cong \frac{M-L+1}{M}I_\mathrm{Ave} \\
&\cong \frac{B_\mathrm{A} - B_\mathrm{I}}{B_\mathrm{A}}I_\mathrm{Ave} \equiv F_\mathrm{S}I_\mathrm{Ave}, \tag{18}
\end{aligned}$$

where I_Ave is the average intensity of frequency components after whitening. We call F_S the stabilization factor. We rewrite the covariance matrix after frequency averaging using a Toeplitz matrix $\mathbf{R}_\mathrm{T}$:

$$\mathbf{R}_\mathrm{A} = F_\mathrm{S}I_\mathrm{Ave}\mathbf{R}_\mathrm{T} + \mathbf{R}', \tag{19}$$

where all the diagonal elements of $\mathbf{R}'$ have positive values. When the covariance matrix becomes a Toeplitz matrix, FDI imaging can estimate the true echo intensity.[20,34] Therefore, the intensity estimated by FDI imaging given by Eq. (11) is also rewritten as

$$\begin{aligned}
P'_\mathrm{CAP}(r) &= \text{minimize } \mathbf{W}^{\mathrm{T}*}_\mathrm{A}\mathbf{R}_\mathrm{A}\mathbf{W}_\mathrm{A} \\
&\geq \text{minimize } F_\mathrm{S}I_\mathrm{Ave}\mathbf{W}^{\mathrm{T}*}_\mathrm{A}\mathbf{R}_\mathrm{T}\mathbf{W}_\mathrm{A} \\
&\quad + \text{minimize } \mathbf{W}^{\mathrm{T}*}_\mathrm{A}\mathbf{R}'\mathbf{W}_\mathrm{A} \\
&\cong F_\mathrm{S}I_\mathrm{True} + \text{minimize } \mathbf{W}^{\mathrm{T}*}_\mathrm{A}\mathbf{R}'\mathbf{W}_\mathrm{A}, \tag{20}
\end{aligned}$$

where I_True is the true echo intensity. Equation (20) indicates that the estimated intensity in the proposed FDI imaging is supposed to be larger than $F_\mathrm{S}I_\mathrm{True}$. These frequency components smooth out the excessive suppression of the echo intensity estimated by the Capon method at the cost of a little range resolution. When $F_\mathrm{S} = 1/3$, the estimated intensity is supposed to be larger than $-4.77\,\mathrm{dB}$ relative to the true echo intensity.

2.3 Reference compound applied to FDI imaging with the Capon method

As US uses broadband signals, the target shape causes large variations in the intensity and phase of each frequency component of a received signal, resulting in a large variation in the echo waveform. FDI imaging with the Capon method assumes that the echo waveform that returned from a single

target resembles the waveform of the reference signal. When the echo waveform that returned from a target is different from the reference waveform, the estimated intensity at the target depth decreases and the target image blurs. Therefore, we used multiple reference signals to satisfy the condition that the echo waveform of each target in a ROI resembled at least one of the reference waveforms. We estimate the intensity of a measurement plane using each reference signal separately, and then average the estimated intensities.

$$P_{\text{CapRC}}(r) = \frac{1}{Q} \sum_{q=1}^{Q} P_{\text{CapR}}(r, q), \qquad (21)$$

where $P_{\text{CapR}}(r, q)$ is the intensity estimated by FDI imaging using the q-th reference signal, and Q is the number of reference signals used. We call this technique the reference compound (RC) technique. When the reference signal resembles the target echo waveform, the intensity profile estimated using the reference signal is supposed to have a sharp and large peak at the target depth. This means that the average of the intensities estimated using the multiple reference signals has the potential to depict target images stably. In addition, the appearance of false images depends on the reference signal used. This implies that RC can have the same effect as the frequency compound in suppressing speckle noise.[32]

In ultrasound imaging of the human carotid artery in a longitudinal section, the vessel wall interfaces are supposed to be flat in the incident region of the ultrasound beam. We thus used multiple flat interfaces with various slope angles as reference targets for vessel wall imaging in the experimental study. This setting neglects the waveform change caused by the measurement depth variation, because this waveform change causes a slight deterioration of image quality.[33]

2.4 Simulation and experimental setup

In the simulation study, we investigate the performance of the proposed method when there are two horizontal interfaces in a ROI, where the waveform that returned from each interface is the same as that of the reference signal. When the received signal includes no noise, the echo that returned from two interfaces is given by

$$s(I_T, t) = s_R(t) + s_R(t - 2I_T/c), \qquad (22)$$

where I_T is the target interval and $s_R(t)$ is the reference signal. We can construct the received signal from sloped interfaces by employing the echo from a sloped interface as the reference signal $s_R(t)$. To investigate the effects of noise in the proposed method, we added white noise to the constructed received signal given by Eq. (22). The signal intensity is the average echo intensity in the −3 dB temporal width of a reference signal, and the noise intensity is the average echo intensity of the received signal in a 2 cm range that includes no echo signal.

Experiments were conducted using a Hitachi EUB-8500 US device with a 7.5 MHz linear array to acquire raw IQ data. The IQ data were converted to RF data, where the sampling frequency of the converted RF data was 30 MHz.[29] The transmit focal depth was 15 mm, and the scan line and range intervals of the US device were about 0.27 and 0.05 mm, respectively. Figure 2 shows the echo waveforms of three interfaces between 20% gelatin and 4% agar at a depth of
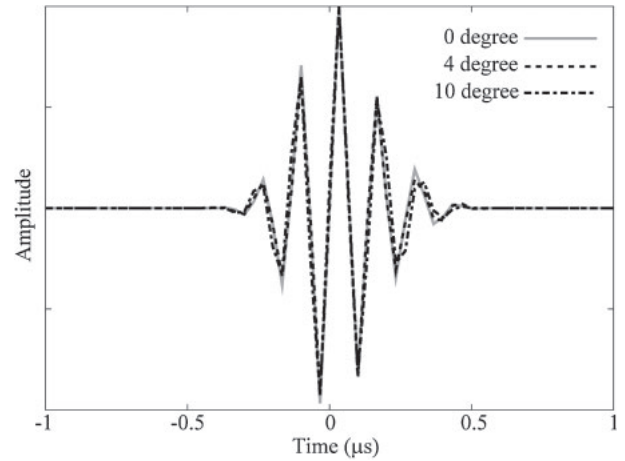

Fig. 2. Echo waveform of an interface between 20% gelatin and 4% agar, where 10 echoes of different scan lines were coherently averaged after arrival time adjustment to suppress noise. The slope angles of the interface are 0, 4, and 10°.

15 mm, which we use as the reference signals. In the determination of each reference signal, we averaged 10 echoes of different scan lines coherently to suppress noise. In the FDI imaging, we used a single-frame US data to depict each image. The −6 dB bandwidth of the echo from the horizontal interface was 2.6 MHz. The half-power width of the ultrasound beam of the US device in the lateral direction was about 0.5 mm at a depth of 1.5 cm. We supposed that the sound velocity was 1500 m/s, and thus the range interval of the RF data was 0.025 mm. We used a rectangular window function of 1 cm width to cut out the received signal in the ROI from the whole signal. Because each signal of a scan line, at depths from 1 to 2 cm, consisted of 400 range samples, the sampling interval in the frequency domain was 75 kHz. In this study, we used bandwidths of 4, 5, and 6 MHz. The corresponding bands were from 5.3 to 9.3 MHz, from 4.8 to 9.8 MHz, and from 4.1 to 10.1 MHz, where the numbers of frequency components N were 54, 68, and 81, respectively. As FDI imaging with the Capon method has a spatial resolution of about 0.05 mm, a range interval of 0.01 mm is adequate for this method.[29] Therefore, we used a range sampling interval of 0.01 mm. The sampling frequency of 30 MHz determines the range sampling interval for the conventional B-mode method of 0.025 mm. We had adjusted the range interval of the B-mode images to 0.01 mm by interpolation.

The optimum stabilization term η in Eq. (1) is proportional to the noise intensity of the k-th frequency component of the received signal when the received signal intensity is equal to the reference signal intensity; however, it is difficult to measure noise intensity because it commonly varies. Therefore, we introduced the assumption we made in our previous work that the expectation of the noise intensity was uniform in all frequency components.[29] In this study, for the value of η, we used the average intensity of the received signal in the band from 11 to 14 MHz, adjusting the average signal intensity of the received signal to that of the reference signal:

$$\eta = I_{\text{RS}} I_{\text{PN}} / I_{\text{PS}}, \qquad (23)$$

where I_{RS} is the average intensity of the reference signal in the band used in the proposed method, and I_{PN} and I_{PS} are the

respective average intensities of the received signal in the band from 11 to 14 MHz and in the band used by the proposed method. I_{RS}/I_{PS} adjusts the average intensity of the received signal to that of the reference signal. Using $\eta'\mathbf{E}$ stabilizes $\mathbf{R}_A^{-1}$ at the cost of a decrease in SNR. As this decrease reduces the image quality of the proposed method, we should use small η' values. In the present study, we used -40 dB of the average value of the diagonal terms of $\mathbf{R}_A$ as the value for η'.[29]

We investigated the accuracy of FDI imaging in measuring the thickness of a vessel wall using a fixed swine femoral arteries embedded in a gelatin block. First, adventitial layers were removed completely from a fresh femoral artery. We followed the methods of our previous work[29] to prepare the fixed gelatin block with the artery and to measure the vessel-wall thickness. First, we measured a longitudinal section of the fixed artery using a commercial US device. After completion of the US measurement, an anatomist immediately cut the gelatin block with a blade inserted into the pair of slits in the cutting case, where the pair of slits was used to adjust the cut section in the imaging plane. This process guaranteed that the cut site was very close to the ultrasound-imaging site. The anatomist traced the vessel wall interfaces microscopically. We subsequently applied the proposed FDI imaging to the received IQ data of six human carotid arteries of three living normal subjects to examine the performance of the proposed method in a clinical situation.

The RC works when multiple reference signals are used, in cases where the echo waveform of each target in a ROI resembles at least one of the reference waveforms. To handle waveform variation due to the varying slope angle of the arterial wall interfaces, we employed six reference signals that returned from flat interfaces between 20% gelatin and 4% agar, with slope angles of 0 to 10 deg in 2-degree steps, as shown in Fig. 2. The center of each interface was located at a depth of 15 mm.

3. Results and discussion

3.1 Range resolution of FDI imaging in a simulation study

We evaluated the performance of FAS, which smoothes out the excessive suppression of the echo intensity estimated by FDI imaging with the Capon method.[31] Figure 3 shows the intensity estimated by conventional B-mode imaging, conventional FDI imaging and FDI imaging with FAS, where the SNR is from 0 to 30 dB, there are two horizontal interfaces in a ROI, and the target interval is 0.2 mm. In this evaluation, we employ FDI imaging without RC. Because the -6 dB bandwidth of the signal used in this simulation study is 2.6 MHz, the conventional B-mode imaging has a range resolution of about 0.3 mm. The conventional FDI imaging allocates one-half of the whole bandwidth for frequency averaging.[29] The conventional FDI imaging has a higher range resolution than the B-mode imaging; however, its performance is unstable at low SNR. FDI imaging with FAS showed the interfaces reliably. FDI images were acquired with a sufficient range resolution using a 2 MHz bandwidth; this result is consistent with those of a previous study.[29] We also employed FDI imaging with FAS, allocating a bandwidth of 3 MHz for frequency averaging from a total bandwidth of 5 MHz. Because the bandwidth for imaging is 2 MHz, the remainder B_A-B_I is 1 MHz for this setting. FDI
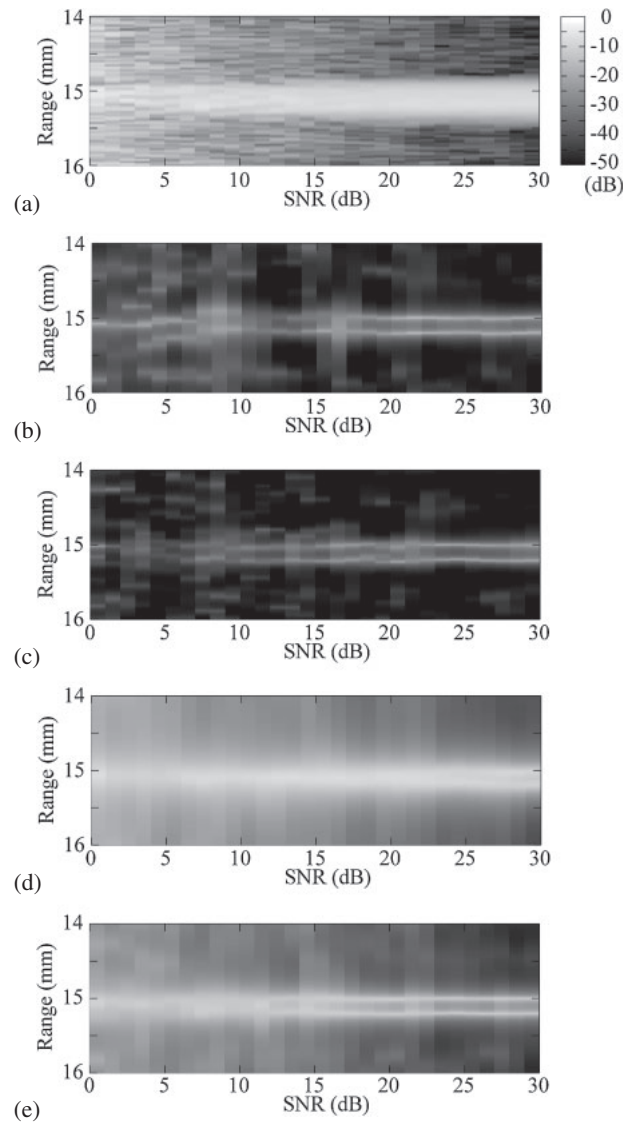

Fig. 3. Estimated intensity as a function of the SNR from 0 to 30 dB when there are two interfaces at depths of 15.0 and 15.2 mm. The intensity profiles are estimated by (a) conventional B-mode imaging, (b) and (c) conventional FDI imaging, and (d) and (e) FDI imaging with FAS. The bandwidth for frequency averaging (B_A) and that for imaging (B_I) are respectively (b) 2 and 2 MHz, (c) 3 and 3 MHz, (d) 3 and 1 MHz, and (e) 3 and 2 MHz.

imaging with FAS is supposed to have high range resolution and greater robustness.

Figure 4 shows the estimated echo intensity of the target interfaces calculated by the conventional FDI imaging and by FDI imaging with FAS, where there are two interfaces at depths of 15.0 and 15.2 mm and the true echo intensity is 0 dB.[31] Our previous study shows that the cross-correlation term is proportional to a sinc function given by Eq. (17). The sinc function is less than 0.25 when $\pi B_A \Delta r/c$ is larger than 2.48. Therefore, the suppression of the cross-correlation term by more than 6 dB requires a constraint on the bandwidth for frequency averaging given by

$$B_A \geq c/2.53 I_{Tmin}, \qquad (24)$$

where I_{Tmin} is the minimum target interval. When the target interval is 0.2 mm, the bandwidth of 3 MHz for frequency averaging is sufficient for the suppression of the cross-correlation term. However, using a wide bandwidth means
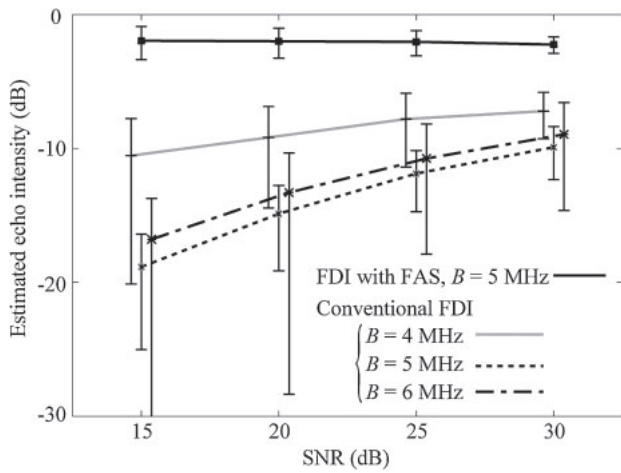
Fig. 4. Estimated echo intensity of target interfaces calculated using the conventional FDI imaging and the FDI imaging with FAS, where there are two target interfaces at depths of 15.0 and 15.2 mm and the true echo intensity is 0 dB. The FDI imaging with FAS allocates a bandwidth of 3 MHz for frequency averaging from a total bandwidth (B) of 5 MHz. The FDI imaging without FAS allocates half bandwidths for frequency averaging from total bandwidths of 4, 5, and 6 MHz. Each error bar denotes the standard deviation, where 10 simulation data with random white noise are used.

using low-SNR frequency-components that makes the conventional FDI imaging unreliable. Because the Capon method minimizes the output power, the unreliable performance of the conventional FDI method results in the underestimation of echo intensity. In contrast, FDI imaging with FAS enabled the estimation of echo intensity with an average estimation error within 2.3 dB and with small variations. Under this condition, the stabilization factor F_S is equal to 1/3. In all cases, the normalized echo intensity estimated by FDI imaging with FAS is larger than −4.77 dB. This result is consistent with the results of the theoretical investigation shown in Sect. 2.2. In a longitudinal section of an artery, the depths and echo intensities of an arterial wall were similar. Therefore, in a B-mode image there was a high lateral continuity at the region of an arterial wall, as shown in Fig. 8. FDI imaging estimates the echo intensities in each scan line separately. Therefore, the low performance of the conventional FDI imaging in estimating echo intensity should increase the variation of the estimated echo intensity of an arterial wall, causing a low lateral continuity at a region of an arterial wall. The high performance of the proposed FDI imaging in echo intensity estimation improved the lateral continuity in a FDI image, as shown in Fig. 8(c). These results indicate the efficiency of FAS in estimating echo intensity and in improving continuity in the lateral direction.

Figure 5 shows the intensity estimated by FDI imaging with and without RC, where the slope angles of the target interfaces are 0 and 10 deg, and the bandwidths for frequency averaging and imaging are 3 and 2 MHz, respectively. Each signal that returned from two interfaces was constructed using Eq. (22), where the signal included no noise. FDI imaging without RC used a single reference signal that returned from a horizontal interface. FDI imaging with RC used six reference signals that returned from six interfaces with slope angles of 0, 2, 4, 6, 8, and 10°. Under high SNR conditions, the conventional FDI imaging and FDI imaging
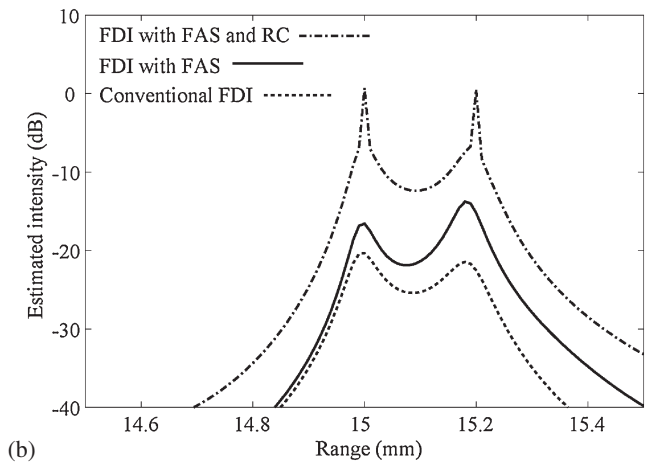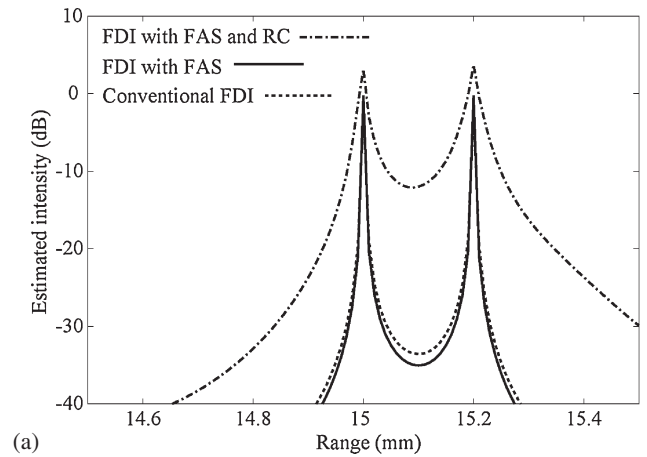

Fig. 5. Intensity of two interfaces estimated by the conventional FDI imaging, the FDI imaging with FAS, and the FDI imaging with FAS and RC, where the slope angles of the two interfaces are (a) 0 and (b) 10°. Each signal that returned from two interfaces was constructed using Eq. (22), where the signal included no noise. The target depths are 15.0 and 15.2 mm.

with FAS estimated similar intensity profiles, as shown in Fig. 5(a). This is consistent with the results shown in Figs. 3(b) and 3(e). FAS improves the accuracy of estimating echo intensity; however, it is insufficient when the slope angle of the target interface is different from that of the reference. Figure 5 indicates that FDI imaging with RC achieves robustness in terms of spatial resolution and echo intensity estimation for various target slope angles.

3.2 Agar phantom images acquired using FDI imaging
We experimentally investigated the performance of the proposed FDI imaging using a 0.15-mm-thick agar membrane phantom, where an anatomist measured the membrane thickness microscopically. Figures 6 and 7 show ultrasound images of an agar membrane phantom acquired using the conventional B-mode imaging, the conventional FDI imaging and the proposed FDI imaging with FAS and RC. Because the conventional B-mode imaging had an image extent of 0.29 mm in the range direction, it failed to depict the pair of interfaces between the 0.15 mm agar membrane and the gelatin. The conventional FDI imaging and the proposed method allocated 2 and 3 MHz for frequency averaging from the total bandwidths of 4 and 5 MHz, respectively. The conventional FDI imaging has a higher spatial resolution than the B-mode imaging; however, its echo intensity estimation
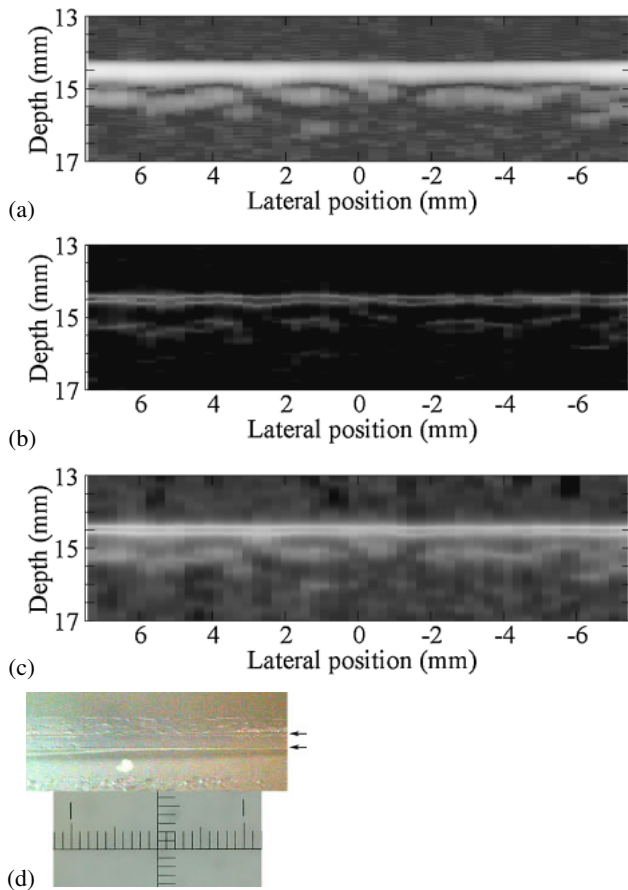
(a)

(b)

(c)

(d)

Fig. 6. (Color online) Ultrasound images of a horizontal agar membrane acquired by (a) a conventional B-mode imaging, (b) the conventional FDI imaging, and (c) the proposed FDI imaging with FAS and RC, and (d) microscopy image of the membrane. The dynamic range of each ultrasound image is 50 dB, and the agar membrane is 0.15 mm thick in the microscopy image. The arrows in the microscopy image indicate the interface between gelatin and agar.

(a)

(b)

(c)

Fig. 7. Ultrasound image of a 10-deg-sloped agar membrane acquired by (a) the conventional B-mode imaging, (b) the conventional FDI imaging, and (c) the proposed FDI imaging with FAS and RC. The dynamic range of each ultrasound image is 50 dB, and the agar membrane is 0.15 mm thick in the microscopy image.

accuracy is lower than that of the B-mode imaging, resulting in low continuity in the lateral direction, as described in our previous work.[29] In contrast, the proposed FDI imaging with FAS and RC showed the pairs of interfaces in front of and behind the horizontal agar membrane and sloped agar membranes. These results are consistent with the performance of FDI imaging shown in Figs. 3(b) and 3(e).

To investigate the performance of the proposed FDI imaging in estimating target depth, we examined 57 scan lines in the 15-mm-wide region in Fig. 6. As shown in Fig. 6(d), the surface of the agar membrane was flat. The median agar membrane thickness estimated using the proposed FDI imaging was 0.17 mm, and the thickness estimation error was 0.02 mm. The average and standard deviation of the depth of the near gelatin-agar interface estimated by the conventional FDI imaging were 14.46 and 0.104 mm, respectively. In contrast, those estimated by the proposed FDI imaging were 14.42 and 0.028 mm, respectively. The standard deviation of the depth estimated using the proposed FDI method was 26.7% of that estimated using the conventional FDI method, indicating the robustness of the proposed imaging method.

We also investigated the underestimation of the proposed FDI imaging at the echo intensity of the near gelatin-agar interface. We examined 57 scan lines in the 15-mm-wide
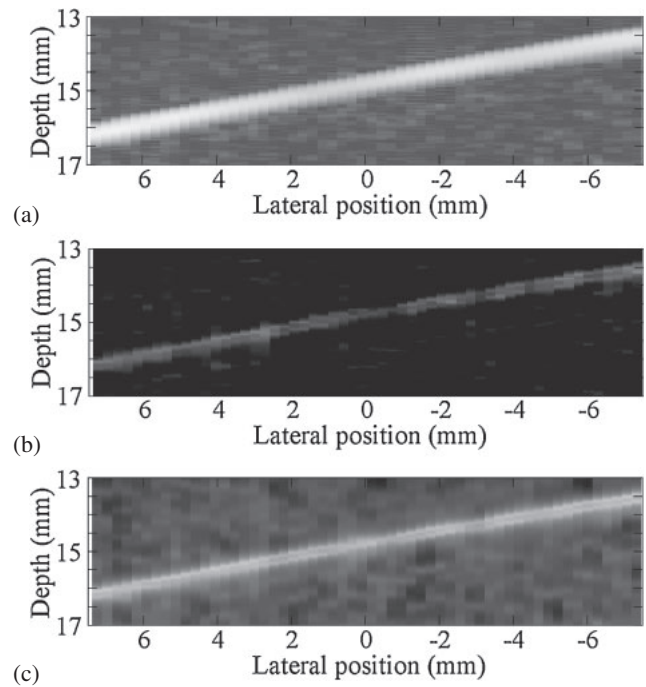
region in Figs. 6 and 7. In the conventional FDI image, 8.8 and 22.8% of all the scan lines had echo intensities lower than one-quarter of the average echo intensity when the slope angles were 0 and 10 deg, respectively. In the proposed FDI image no scan line had an echo intensity lower than one-quarter of the average echo intensity in both cases. This result indicates the efficiency of the proposed techniques in acquiring robustness.

3.3 Images of swine femoral arteries acquired using FDI imaging

We experimentally investigated the performance of the proposed FDI imaging using a fixed swine femoral artery. Figure 8 shows ultrasound images of a longitudinal section of a fixed swine femoral artery acquired using the conventional B-mode imaging, the conventional FDI imaging, and the proposed FDI imaging. The conventional FDI imaging has higher range resolution than the conventional B-mode imaging; however, it also has low continuity in the lateral direction. In contrast, the proposed FDI imaging has both high range resolution and good continuity in the lateral direction.

We investigated the underestimation of the proposed FDI imaging at the echo intensity of the far-wall lumen–intima interface. We examined 57 scan lines in the 15-mm-wide region in Fig. 8. In the conventional FDI image, 19.3% of all the scan lines had echo intensities lower than one-quarter of the average echo intensity. In the proposed FDI image, 5.3% had low echo intensities. This result also indicates the efficiency of the proposed techniques in acquiring robustness.

Figure 9 shows the interfaces at the posterior wall of a fixed swine femoral artery acquired using the proposed FDI imaging, where the interfaces were projected onto a
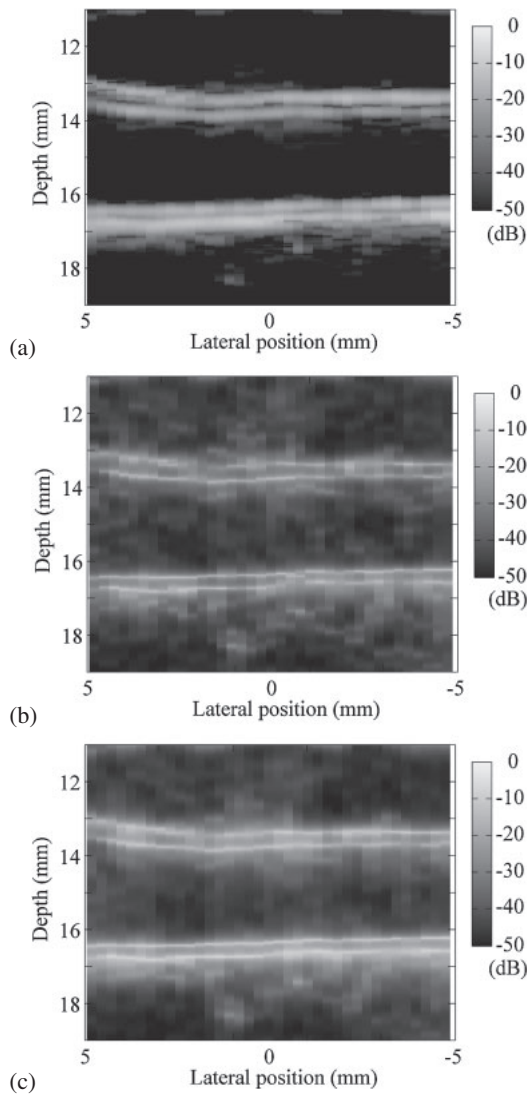
Fig. 8. Ultrasound images of a fixed swine femoral artery acquired using (a) the B-mode imaging, (b) the conventional FDI imaging without FAS and RC, and (c) the proposed FDI imaging with FAS and RC.

Fig. 9. (Color online) Interfaces depicted at the posterior wall in an FDI image projected onto a corresponding microscopy image on a millimeter scale. Red lines indicate a lumen–intima interface and a media-adventitia interface traced histologically. Blue broken lines indicate the interfaces depicted in the proposed FDI image using FAS and RC.

Fig. 10. Interpolated B-mode image of a normal living human carotid artery in vivo obtained using a commercial ultrasonographic device. Images were acquired using (a) the B-mode imaging, (b) the conventional FDI imaging, and (c) the proposed FDI imaging with FAS and RC.

corresponding microscopy image. For this study, we investigated 20 scan lines in the 5-mm-wide central region in Fig. 9. The interfaces shown using the proposed FDI imaging were sufficiently close to those traced microscopically. In this investigation, we selected two peak positions in the region 1 mm deep in the posterior arterial wall for each scan line of the ultrasound images. When there was only one peak intensity position or the interval between the two peak positions was not within the range from 0.20 to 0.50 mm, we determined that a complete failure had occurred at the scan line, and excluded the scan line from the calculation of the average and the standard deviation of arterial wall thickness. The complete failure occurrence ratios were 5, 10, and 5% in the B-mode, conventional FDI, and proposed FDI images, respectively. The average and the standard deviation of arterial wall thickness measured microscopically were 0.3217 and 0.0128 mm, respectively, and the results estimated using the proposed FDI imaging were 0.3242 and 0.0232 mm, respectively. In contrast, those estimated using the B-mode imaging were 0.3100 and 0.0316 mm, respectively. These results show the high performance of the proposed FDI imaging in depicting arterial walls.
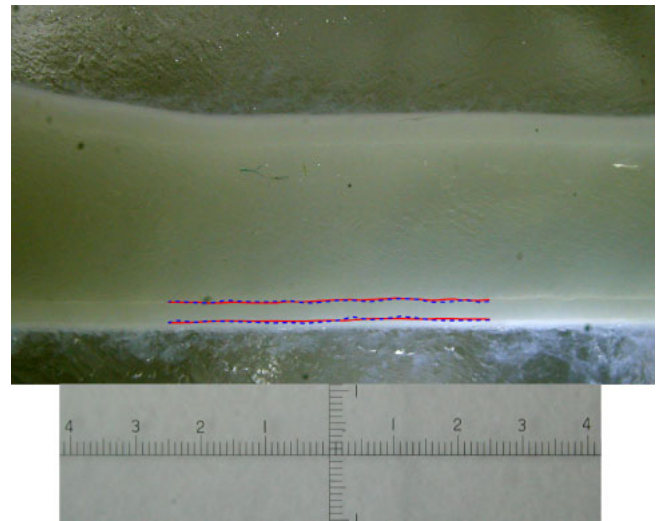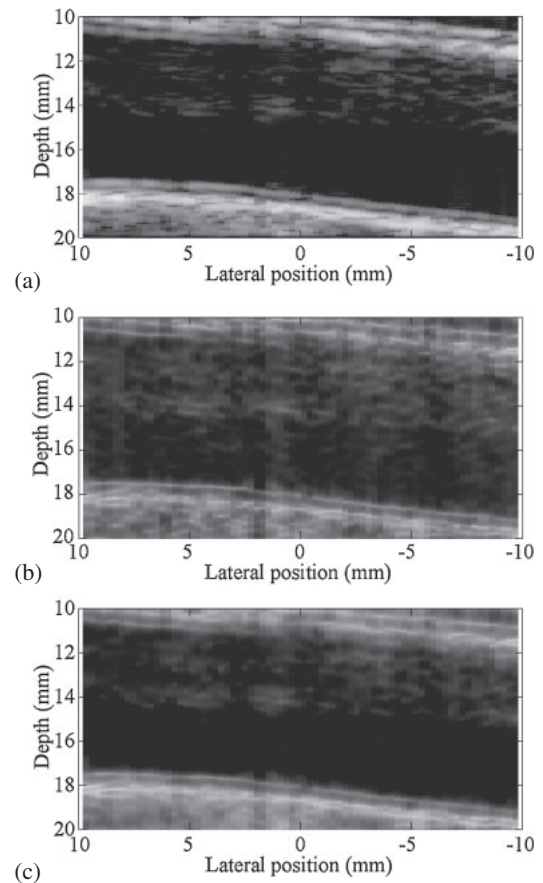
3.4 High-range-resolution ultrasound imaging of a human carotid artery in vivo

We applied the proposed FDI imaging with FAS and RC to raw IQ data of six carotid arteries in vivo, where each FDI image was constructed from single-frame IQ data. Figure 10
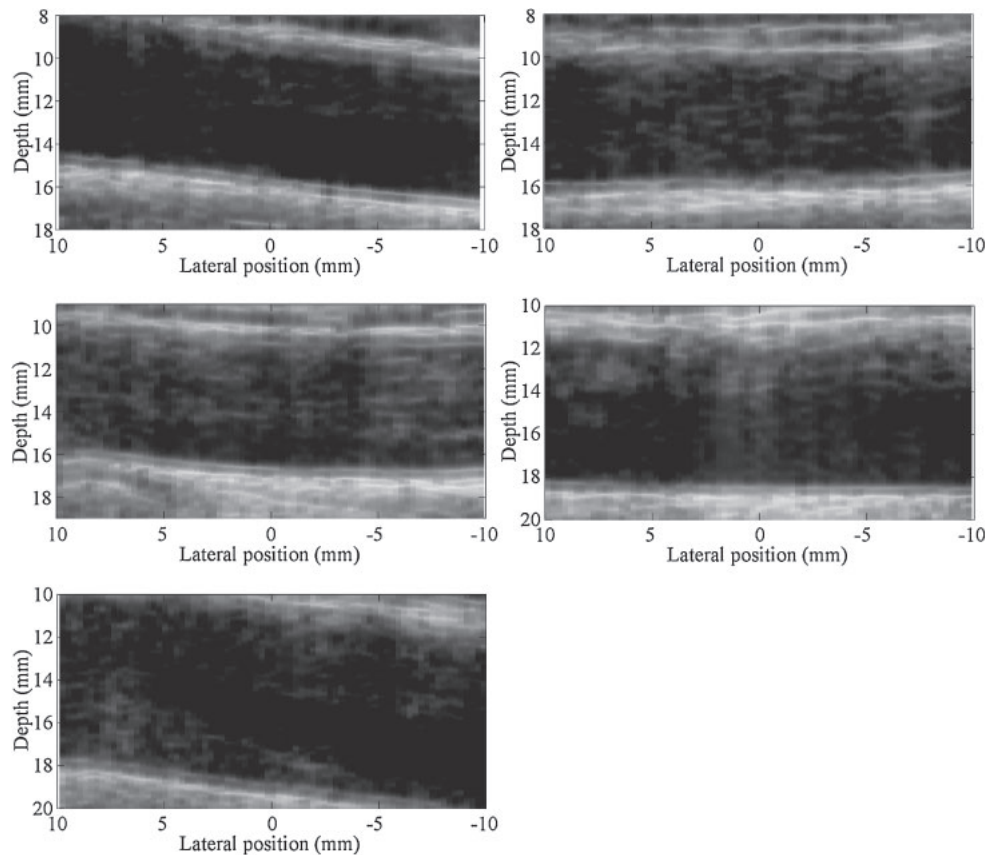
Fig. 11. Ultrasound images of five normal living human carotid arteries in vivo depicted using the proposed FDI imaging. This method is applied to a single frame of IQ data obtained using a commercial ultrasonographic device.

shows ultrasound images of a human carotid artery in vivo acquired using the B-mode imaging, conventional FDI imaging and proposed FDI imaging. The proposed FDI method also provided high-range-resolution images of this artery and the five other human carotid arteries used in this study. These results verify that the proposed method can stably acquire a high-range-resolution image of normal living human carotid arteries. Figure 11 shows images of the other human carotid arteries obtained using the proposed FDI method. These results verify that the proposed method enabled the stable acquisition of a high-range-resolution image of a normal living human carotid artery. The calculation time for a ROI of 1×2 cm (i.e., 1001 range samples $\times$ 75 scan lines) was approximately 0.06 s/frame, and the calculations were performed using a desktop PC with a single CPU (Intel Xeon 3.33 GHz) and 6 GB RAM. This result shows that the proposed FDI imaging is suitable for real-time high-resolution vascular ultrasound imaging.

4. Conclusions

We reported a high-range-resolution FDI imaging employing FAS and RC. FAS ensures the robust depiction of artery interfaces when there is a thin layer close to the arterial wall. The RC technique uses multiple reference signals to suppress the deterioration of the imaging performance caused by variation in the echo waveform. The proposed FDI imaging could depict a horizontal 0.15-mm-thick agar membrane stably, and the standard deviation of the estimated depth was suppressed to 26.7% of that obtained using the conventional FDI method. The proposed method also succeeded in suppressing the underestimation of the echo intensity effectively, and in the observation of an agar membrane and a swine artery from 0 to 5.3% of the scan lines with echo intensities lower than one-quarter of the average echo intensity, where 8.8 to 22.8% of the scan lines had low echo intensities when a conventional FDI method was employed. The proposed method also enabled the acquisition of high-range-resolution images of six living human carotid arteries. The proposed method required 0.06 s/frame using a desktop PC with a single CPU for a ROI of 1×2 cm. These results indicate that the proposed FDI imaging has the potential to produce real-time high-range-resolution ultrasound vascular images that will enable major improvements in ultrasound medical diagnoses.

1) J. W. Levenson, P. J. Skerrett, and J. M. Gaziano, Prev. Cardiol. **5**, 188 (2002).
2) D. Asari, H. Hasegawa, and H. Kanai, Jpn. J. Appl. Phys. **53**, 07KF21 (2014).
3) Y. Fujita, H. Tagashira, H. Hasegawa, K. Fukunaga, and H. Kanai, Jpn. J. Appl. Phys. **53**, 07KF25 (2014).
4) H. Takahashi, H. Hasegawa, and H. Kanai, Jpn. J. Appl. Phys. **53**, 07KF08

(2014).

5) H. Hasegawa and H. Kanai, Jpn. J. Appl. Phys. **53**, 07KF02 (2014).

6) M. Petretta and A. Cuocolo, Atherosclerosis **223**, 95 (2012).

7) M. Rosenkranz, A. Russjan, E. Goebell, S. Havemeister, G. Thomalla, B. Cheng, C. Beck, A. Krützelmann, J. Fiehler, and C. Gerloff, Cerebrovasc. Dis. **32**, 163 (2011).

8) Y. Nagai, H. Hasegawa, and H. Kanai, Jpn. J. Appl. Phys. **53**, 07KF19 (2014).

9) M. Juonala, M. Kähönen, T. Laitinen, N. Hutri-Kähönen, E. Jokinen, L. Taittonen, M. Pietikäinen, H. Helenius, J. S. A. Viikari, and O. T. Raitakari, Eur. Heart J. **29**, 1198 (2008).

10) F. Núñez, C. Martínez-Costa, J. Sánchez-Zahonero, J. Morata, F. J. Chorro, and J. Brines, Rev. Esp. Cardiol. **63**, 1253 (2010).

11) M. Sato, H. Hasegawa, and H. Kanai, Jpn. J. Appl. Phys. **53**, 07KF03 (2014).

12) H. R. Reynolds, D. A. Steckman, P. A. Tunick, I. Kronzon, I. Lobach, and B. P. Rosenzweig, Am. Heart J. **159**, 1059 (2010).

13) D. H. O'Leary and D. H. Bots, Eur. Heart J. **31**, 1682 (2010).

14) H.-P. Brunner-La Rocca, Eur. Heart J. **31**, 2320 (2010).

15) S. P. Weinstein, E. F. Conant, and C. Sehgal, Semin. Ultrasound CT MR **27**, 273 (2006).

16) J. Capon, Proc. IEEE **57**, 1408 (1969).

17) W. F. Gabriel, Proc. IEEE **68**, 654 (1980).

18) B. Widrow, K. Duvall, R. P. Gooch, and W. Newman, IEEE Trans. Antennas Propag. **30**, 469 (1982).

19) T. J. Shan and T. Kailath, IEEE Trans. Acoust. Speech Signal Process. **33**, 527 (1985).

20) K. Takao and N. Kikuma, IEEE Trans. Antennas Propag. **35**, 1389 (1987).

21) J. A. Mann and W. F. Walker, Proc. IEEE Ultrason. Symp. 2002, p. 1807.

22) J.-F. Synnevåg, A. Austeng, and S. Holm, IEEE Trans. Ultrason. Ferroelectr. Freq. Control **56**, 1868 (2009).

23) J.-F. Synnevåg, A. Austeng, and S. Holm, IEEE Trans. Ultrason. Ferroelectr. Freq. Control **57**, 281 (2010).

24) F. Lingvall, Ultrasonics **42**, 961 (2004).

25) F. Viola, M. A. Ellis, and W. F. Walker, IEEE Trans. Med. Imaging **27**, 99 (2008).

26) H. Luce, M. Yamamoto, S. Fukao, D. Helal, and M. Crochet, J. Atmos. Sol.-Terr. Phys. **63**, 221 (2001).

27) J. M. Schmitt, IEEE J. Sel. Top. Quantum Electron. **5**, 1205 (1999).

28) H. Taki, K. Taki, T. Sakamoto, M. Yamakawa, T. Shiina, and T. Sato, Proc. IEEE EMBS, 2010, p. 5298.

29) H. Taki, K. Taki, T. Sakamoto, M. Yamakawa, T. Shiina, M. Kudo, and T. Sato, IEEE Trans. Med. Imaging **31**, 417 (2012).

30) H. Taki, T. Sakamoto, M. Yamakawa, T. Shiina, and T. Sato, IEEJ Trans. Electron. Inf. Syst. **132**, 1552 (2012).

31) H. Taki, K. Taki, T. Sakamoto, M. Yamakawa, T. Shiina, M. Kudo, and T. Sato, Proc. IEEE EMBS, 2014, p. 5085.

32) H. Taki, T. Sakamoto, M. Yamakawa, T. Shiina, T. Sato, K. Taki, and M. Kudo, Proc. IEEE Ultrasonics Symp., 2011, p. 2201.

33) H. Taki, T. Sakamoto, K. Taki, M. Yamakawa, T. Shiina, M. Kudo, and T. Sato, Proc. IEEE EMBS, 2013, p. 1398.

34) H. Taki, T. Sakamoto, M. Yamakawa, T. Shiina, T. Sato, K. Taki, and M. Kudo, Proc. IEEE Ultrasonics Symp., 2013, p. 805.